Toughening of Composite Interfaces for Damage Resistance with Nanoparticle Interleaves

Subramanian, Nithya; Bisagni, Chiara

DOI
10.3390/jcs9030109

Publication date
2025

Document Version
Final published version

Published in
Journal of Composites Science

Citation (APA)
Subramanian, N., & Bisagni, C. (2025). Toughening of Composite Interfaces for Damage Resistance with Nanoparticle Interleaves. *Journal of Composites Science*, *9*(3), Article 109. https://doi.org/10.3390/jcs9030109

Journal of
Composites Science

MDPI

Article

Toughening of Composite Interfaces for Damage Resistance with Nanoparticle Interleaves

Nithya Subramanian [1,2] and Chiara Bisagni [1,3,*]

[1] Faculty of Aerospace Engineering, Delft University of Technology, 2629 HS Delft, The Netherlands; nithya.subramanian@tno.nl
[2] TNO (Netherlands Organisation for Applied Scientific Research), 6167 RD Geleen, The Netherlands
[3] Department of Aerospace Science and Technology, Politecnico di Milano, 20156 Milan, Italy
* Correspondence: chiara.bisagni@polimi.it

Abstract: Composite interfaces, particularly in joints, play a critical role in the damage resistance and durability of structures for aeronautics applications. This study investigates the use of carbon nanotube (CNT) interleaves for the co-cured joining of composite parts and its effects on fracture toughness and damage progression at the co-cured interface. CNT dispersed in a thermoset resin and partially cured into thin film interleaves at three weight concentrations (0.5% wt., 1% wt., and 2% wt.) of two discrete thicknesses (200 µ and 500 µ) were investigated. The fracture toughness of the co-cured interface with CNT interleaves in mode I and mode II loading conditions was determined through double cantilever beam and end-notched flexure tests, respectively. The results reveal that despite the occurrence of a stick–slip damage progression in mode I, the crack arrest mechanisms and forces are surprisingly predictable based on interleaf thickness. At CNT concentrations above 1% wt., there was no significant enhancement of toughening, and interleaf thickness controlled the crack arrest loads. Damage delay also occurred at the interface due to the activation of multiscale toughening mechanisms. Toughening in mode II was dominated by CNT pullout resistance and, therefore, yielded up to six-fold improvement in critical fracture toughness. These insights offer significant potential for designing joints with nanocomposites for aerospace applications, incorporating inherent toughening and damage delay mechanisms.

Keywords: carbon nanotubes; damage arrest; film interleaves; fracture toughness; co-cured interface

check for updates

Academic Editor: Vincenzo Fiore

Received: 25 January 2025
Revised: 18 February 2025
Accepted: 24 February 2025
Published: 26 February 2025

Citation: Subramanian, N.; Bisagni, C. Toughening of Composite Interfaces for Damage Resistance with Nanoparticle Interleaves. *J. Compos. Sci.* **2025**, *9*, 109. https://doi.org/10.3390/jcs9030109

1. Introduction

In aeronautical applications, the joining of composite structures is crucial because it ensures the integrity and reliability of lightweight components, which must withstand extreme conditions and stresses. Composite structures are typically joined using adhesive co-bonding [1], co-curing [2], or mechanical fastening. Mechanical fastening involves drilling holes that cut through fibers, leading to stress concentrations, an increased part count, and added structural weight. Adhesive co-bonding minimizes stress concentrations but can introduce weak interfaces that are prone to delamination under certain loading and environmental conditions [2]. Co-curing often provides a strong seamless bond and reduces the number of parts; however, it requires precise control and alignment of the parts throughout the curing process, which can be complex [3].

In co-cured joining, interleaved composite laminates with a flexible film layer between joining surfaces improve damage tolerance and delamination resistance by creating larger plastic zones and tortuous crack paths [4–6]. A partially cured epoxy film as an interleaf ensures uniform thickness and prevents misalignments by restraining relative sliding during lay-up, thus simplifying the integration of the co-curing layer and making it suitable for automated manufacturing.

Research over the past two decades has explored how dispersed and aligned carbonaceous nanoparticles (graphene platelets, nanotubes, etc.) enhance the mechanical and multifunctional properties of polymers [7–10]. Studies on carbon nanotube (CNT)-reinforced thermoset polymers have shown improved toughness [11,12] through mechanisms such as crack deflection [13], crack pinning [14], CNT pullout [15], and microscale and nanoscale crack bridging with larger fracture process zones. These mechanisms require interactions between the crack front and the CNT. Recent studies suggest that adding CNT in a targeted fashion with controlled nanoparticle network morphology can trigger/activate multiscale damage suppression, outperforming the homogenous dispersion of nanoparticles [13,16,17]. An investigation demonstrated a 10% improvement in the interlaminar shear strength of hierarchically engineered CNT arrays in aerospace-grade composites [18]. These findings support the idea of incorporating CNT in targeted areas to maximally leverage their benefits as nanoscale reinforcements.

Another equally important aspect is the optimal concentration of CNT that yields benefits to the mechanical behavior of nanocomposites. A related previous study involving molecular simulations of a CNT-dispersed matrix showed that the elastic mechanical properties of the nanocomposite can be improved by adding CNT at up to 2% wt. Weight concentration levels beyond 2% wt. could interfere with the epoxy crosslinking process and lead to the deterioration of mechanical properties [7].

Motivated by the effectiveness of nanoparticles on toughening composites and their potential for expanded applications in co-cured composite joints [19], this paper explores the role of partially cured interleaves containing CNT in co-cured interfaces to arrest and delay damage propagation by allowing the CNT to directly interact with the crack front. This targeted reinforcement approach is preferred over the option of dispersing the CNT in the entire matrix phase of the composite. Neat epoxy interleaves containing no nanoparticles as baseline, CNT loading levels of up to 2% wt. in the epoxy as interleaves, and two different interleaf thicknesses are considered, and their effects on damage propagation mechanisms are studied. Damage mechanisms are inspected in the interleaf from experiments performed under mode I and mode II loads with double cantilever beam (DCB) and end-notched flexure (ENF) specimens, respectively. Following the mechanical tests, in order to investigate the type of interfacial failure (adhesive/cohesive), microcracking in the interleaf, and migration of the crack path, the fracture surfaces are examined with confocal and scanning electron microscopy.

2. Materials and Methods

The materials used for this study, the manufacturing steps, the test setup, and the data analysis schemes are described in the following sub-sections.

2.1. Materials

Three different material systems were used in this study: carbon fiber-based prepreg, neat epoxy resin interleaves, and CNT-modified epoxy interleaves. The prepreg was unidirectional carbon IM7 fiber with a HexPly® 8552 (Hexcel Corporation, Stamford, CT, USA) epoxy resin system with a ply thickness of 0.13 mm. Neat epoxy interleaves (0% wt. CNT) were manufactured with API-60 epoxy—an aerospace-grade resin with a thermal cure cycle and properties compatible with the proprietary HexPly® 8552 resin system. CNT-modified film interleaves from NanoSperse (Kettering, OH, USA) possessed the same host epoxy matrix at three nanoparticle concentrations (0.5% wt., 1% wt., and 2% wt.) and two interleaf thicknesses (200 µ and 500 µ).

2.2. Laminate Manufacturing with Interleaves

The laminate specimens in this study consisted of a unidirectional lay-up with an interleaf co-cured at the midplane: $[0^\circ_{12}/\text{interleaf}/0^\circ_{12}]$. The interleaves were partially cured into a flexible film before their inclusion in the lay-up. The neat epoxy interleaf was staged (partially cured) in the oven between flat glass slabs covered with Teflon backing films for easy removal of the interleaf. The CNT interleaves were already embedded in gloss paper backing films by the manufacturer, and they were staged in the oven on a flat plate. Staging cycles were designed based on cure kinetics characterization via differential scanning calorimetry [4] to attain a resulting degree of cure between 0.3 and 0.35, which is suited for easy handling, ensuring the film was not too fluid but also not overcured before the co-curing process.

For the neat epoxy, the staging cycle involved a heating rate of 1 °C per minute to 110 °C, followed by an isothermal phase at 110 °C for 40 min and subsequent cooling to room temperature at 1 °C per minute. A similar cycle was designed for the CNT interleaf involving a heating rate of 2 °C per minute to 130 °C and an isothermal stage lasting 55 min in the oven. The partially cured interleaves were cooled, peeled from their backing films, and embedded in the midplane of the laminate lay-up. Figure 1a,b show the interleaves after peeling from the backing film, and Figure 1c shows their consolidation in between the two half-laminates, which were cured together in the autoclave.

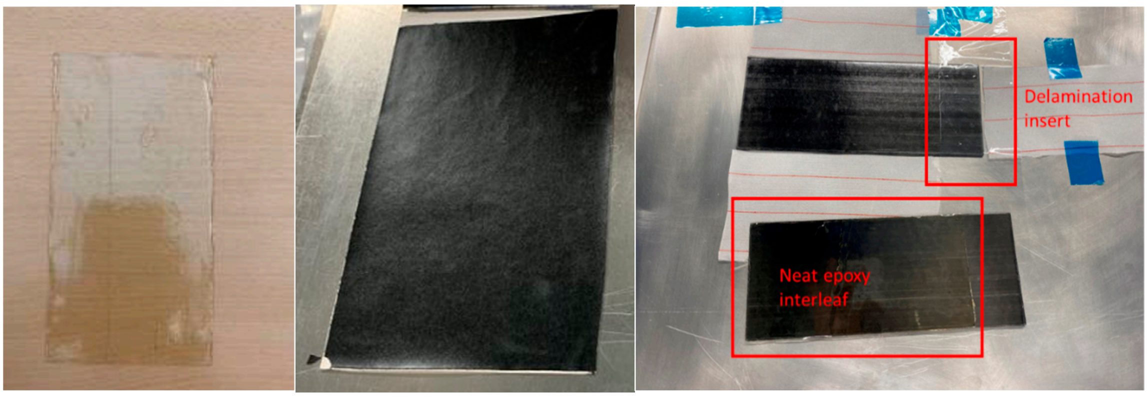

(**a**) (**b**) (**c**)

Figure 1. Manufacturing and consolidation of the interleaf in between the half-laminates. (**a**) Partially cured neat epoxy interleaf (200 µ thickness). (**b**) Partially cured CNT interleaf (0.5% wt. and 200 µ thickness). (**c**) Integration of a neat epoxy interleaf in the laminate midplane adjacent to the Teflon delamination insert. Subfigures adapted from [19].

The initial delamination was embedded in the midplane of the laminate spanning 35 mm using a Teflon release film of 25 µ thickness. During laminate consolidation, the interleaf was introduced at the edge where the Teflon delamination insert ended, as illustrated in Figure 1c. This ensured contact between the crack front and the interleaf layer, as confirmed with subsequent microscopy. The co-cured plates were trimmed and cut into samples in accordance with ASTM standards for DCB and ENF specimens (160 mm length and 25 mm width) with a diamond-tipped circular saw for the fracture toughness tests. The thickness of the specimens varied between 3.3 and 3.8 mm depending on the embedded interleaf thickness.

Table 1 lists the samples tested and their corresponding nomenclature. The nomenclature reflects the type, concentration, and thickness of the interleaf. Plate 1 contained a 200 µ neat epoxy interleaf and yielded two usable samples, whereas the other plates containing CNT interleaves yielded three samples each. Plates 2 and 3 contained interleaves with 0.5% wt. CNT of 200 µ and 500 µ thickness, respectively. Similarly, plates 4 through 7 were manufactured with increasing concentrations of CNT and with each concentration in two discrete thickness interleaves.

Table 1. Number of samples and nomenclature based on interleaf type and thickness.

Plate No.	Interleaf Thickness [µ]	CNT Conc. [% wt.]	Nomenclature	
			DCB (# of Samples)	ENF (# of Samples)
1	200	0 (Neat)	Neat200µDCB (2)	Neat200µENF (2)
2	200	0.5	0.5%CNT200µDCB (3)	0.5%CNT200µENF (3)
3	500	0.5	0.5%CNT500µDCB (3)	0.5%CNT500µENF (3)
4	200	1	1%CNT200µDCB (3)	1%CNT200µENF (3)
5	500	1	1%CNT500µDCB (3)	1%CNT500µENF (3)
6	200	2	2%CNT200µDCB (3)	2%CNT200µENF (3)
7	500	2	2%CNT500µDCB (3)	2%CNT500µENF (3)

2.3. Test Setup

The samples were tested in mode I and mode II loading conditions according to ASTM D5528 [20] and ASTM D7905 standards [21], respectively, to calculate fracture toughness values and plot the delamination resistance curve (R-curve).

2.3.1. DCB Tests

The DCB tests were performed with piano hinges of 20 mm width to link the sample to the load frame. All fracture tests were performed on a Zwick tension/compression test frame with 10 kN maximum capacity. The load frame was attached to a 1 kN load cell for the DCB tests due to lower expected forces. The samples in mode I were loaded at a constant crosshead displacement of 0.3 mm/min. All samples were pre-cracked using the prescribed pre-cracking technique in ASTM D5528 to achieve an initial crack length (a_0) between 28 and 32 mm.

2.3.2. ENF Tests

The ENF tests were performed on a standard 3-point bending fixture, and the 10 kN load cell was used in the Zwick tension/compression test frame. The support rollers in the test setup had a diameter of ~5 mm, and the central loading roller had a diameter of ~9 mm. The distance between the two support rollers was held constant at 100 mm, and the loading rate was controlled by a crosshead displacement of 0.3 mm/min. Compliance calibration (CC) was performed on the non-pre-cracked samples performed with crack lengths of 20, 30, and 40 mm, as recommended in ASTM D7905. During the CC step, the samples were loaded under constant displacement up to a force of 200 N and then unloaded. This CC step does not cause any delamination or crack growth. Following this, the specimens were pre-cracked in mode II first to obtain an initial crack length of 40 mm. Subsequently, fracture tests from the pre-cracked front were performed with an initial crack length of 30 mm by adjusting the overhanging section of the sample beyond the rollers.

The schematics of both test setups are illustrated in Figure 2.

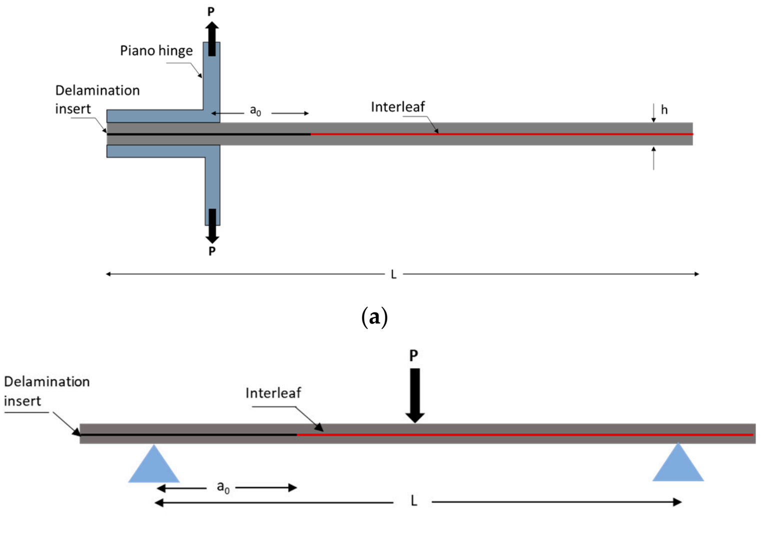

(**a**)

(**b**)

Figure 2. Schematics of test setups: (**a**) DCB test for mode I and (**b**) ENF test for mode II.

2.3.3. Image Acquisition

The sample faces were painted white. One face was marked with two points exactly 40 mm apart (as shown in Figure 3a,c) to measure the crack length with an image processing code. On the other face, 1 mm markings were made in black ink to track crack length propagation visually, as seen in Figure 3b,d. Images from two monochromatic cameras perpendicular to the longitudinal axis of the samples were acquired every second to monitor the crack length. The images from the two cameras were also helpful in determining if the crack front was asymmetric, resulting in different crack lengths on either side during crack propagation.

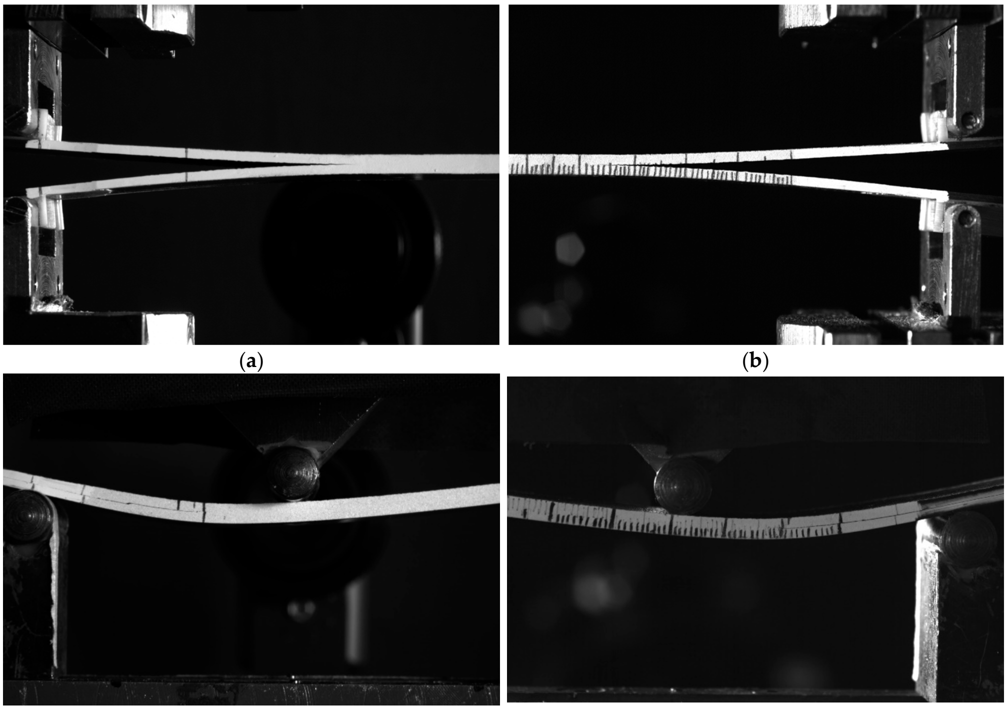

(**a**) (**b**)

(**c**) (**d**)

Figure 3. Images of the sample captured using monochromatic cameras: (**a**) DCB specimen from camera 1; (**b**) DCB specimen from camera 2; (**c**) ENF specimen from camera 1; and (**d**) ENF specimen from camera 2. (**b**) adapted from [19].

2.4. Data Reduction and Analysis

The choice of data reduction techniques among options recommended in the testing standards for modes I and II is detailed in this section.

2.4.1. DCB Tests

Several data reduction methods of the force-displacement ($P - \delta$) data are outlined in ASTM D5528 for determining mode I interlaminar fracture toughness. The modified beam theory (MBT) approach is recommended for materials that exhibit linear elastic fracture, and it also yields the most conservative fracture toughness values. Since MBT is only suitable for interfaces with little plastic deformation, this approach was not chosen to calculate fracture toughness but only to compute the elastic flexural stiffness in our study. A correction to the crack length a, to account for crack tip rotation from the bending of the DCB specimen, was introduced via an additional crack length Δ. The flexural stiffness of the laminate (E_{1f}) could be computed with specimen dimensions (b, h), the measured instantaneous crack length a, the force-displacement data, and Δ, which is the intercept of the linear fit between $C^{1/3}$ and crack length a. This flexural stiffness of the laminate, which is a quantity independent of crack length, was calculated using Equation (1) and used to verify the validity of the experiments by making sure that its value remained constant with crack propagation.

$$E_{1f} = \frac{64P(a + |\Delta|)^3}{\delta b h^3} \tag{1}$$

Another data reduction scheme to compute mode I interlaminar fracture toughness from the force-displacement data from the test machine, as well as the crack lengths from the captured images, is the modified compliance calibration (MCC) approach. In this approach, a least squares plot of the crack length normalized by sample thickness (a/h) as a function of the cube root of compliance ($C^{1/3}$) is generated, and the slope of this fit corresponds to A_1. Since in this study, the samples from different plates possess varying thicknesses, due to the thickness of the embedded interleaf, the MCC approach was chosen because it allowed us to explicitly account for the thickness differences among the samples. It also provides accurate values for mode I interlaminar fracture toughness G_I (through Equation (2)) for materials with significant plastic zones.

$$G_I = \frac{3P^2C^{2/3}}{2A_1 b h} \tag{2}$$

The critical initiation interlaminar fracture toughness G_{Ic} was computed by using the critical initiation load P_{crit}, i.e., the force at which the first crack growth was observed, instead of P in Equation (2). The same approach was used to generate the R-curve, an indicator of the resistance of the interface to crack propagation.

Crack propagation involves the formation of a fracture process zone ahead of the visible crack tip. The size of this process zone sheds light on nonlinear material failure behavior such as void nucleation, crack deflection, microcrack formation, etc. The effective crack length (a_{eff}), which includes the visually observable crack length, a, and the process zone ahead of it, a_{fp}, was calculated using Equation (3) with the tensile modulus of the laminate along the fiber direction E_{11}, the specimen dimensions, and the compliance $C = \delta/P$ from test data. The E_{11} values for the samples in this study strongly depend on the nanoparticle concentration and were therefore obtained from the flexural modulus E_{1f} computed directly via Equation (1) since separate tensile tests were not performed on the sample sets.

$$a_{eff} = a + a_{fp} = \frac{h}{2}\sqrt[3]{(E_{11} b C)} \tag{3}$$

2.4.2. ENF Tests

The standard ENF tests require the compliance calibration step of non-pre-cracked samples and subsequent fracture tests on pre-cracked samples. The compliance calibration coefficients (A, m) were determined using a linear least squares regression analysis of the compliance ($C = \delta/P$), from the force-displacement data of each of the CC tests, versus the crack length cubed (a^3) in the form:

$$C = A + ma^3 \tag{4}$$

Subsequently, the critical shear mode II fracture toughness was calculated as recommended in ASTM D7905 from pre-cracked samples based on Equation (5) using the CC coefficients from Equation (4). In Equation (5), P_{max} corresponds to the maximum force measured during the fracture test, a_{PC} is the crack length, and b is the width of the specimen.

$$G_{IIc} = \frac{3mP_{max}^2 a_{PC}^2}{2b} \tag{5}$$

3. Results and Discussion

The results from the DCB and ENF tests and microscopic characterization of the fracture surfaces are presented.

3.1. Mode I DCB Test

The results of DCB tests are organized based on crack growth stability, underlying crack arrest mechanisms, and R-curve effects, supported by insights from microscopy images.

3.1.1. Stability of Crack Propagation

Figure 4 depicts the force-displacement curves obtained from the Zwick test frame for a representative sample from each set described in Table 1. The data in Figure 4 are organized based on the nanoparticle content and compared to the neat epoxy interleaved laminate in each case. Table 2 presents the critical initiation load values P_{crit} for each sample set and the variation among them. The P-δ profile of the neat epoxy interleaf sample exhibits stable and steady crack propagation, as evidenced by the continuous reduction in the load, subsequent to reaching the maximum force. However, the inclusion of nanoparticles in the interface remarkably alters the force-displacement profiles and underlying damage mechanisms. In each case, the addition of nanoparticles leads to a significant increase in the failure initiation load of the sample, as shown in Table 2. The overall strain energy (area under the curve) is higher than the baseline laminate (with the neat epoxy interleaf), even at low wt. contents of CNT.

Table 2. Critical initiation load values of DCB test samples.

Sample	Mean P_{crit} $[N]$	Std. Deviation $[\sqrt{N}]$
Neat200µDCB	65.41	8.55
0.5%CNT200µDCB	90.59	8.01
0.5%CNT500µDCB	91.44	5.51
1%CNT200µDCB	99.90	11.71
1%CNT500µDCB	120.80	21.66
2%CNT200µDCB	97.61	1.24
2%CNT500µDCB	121.37	5.34

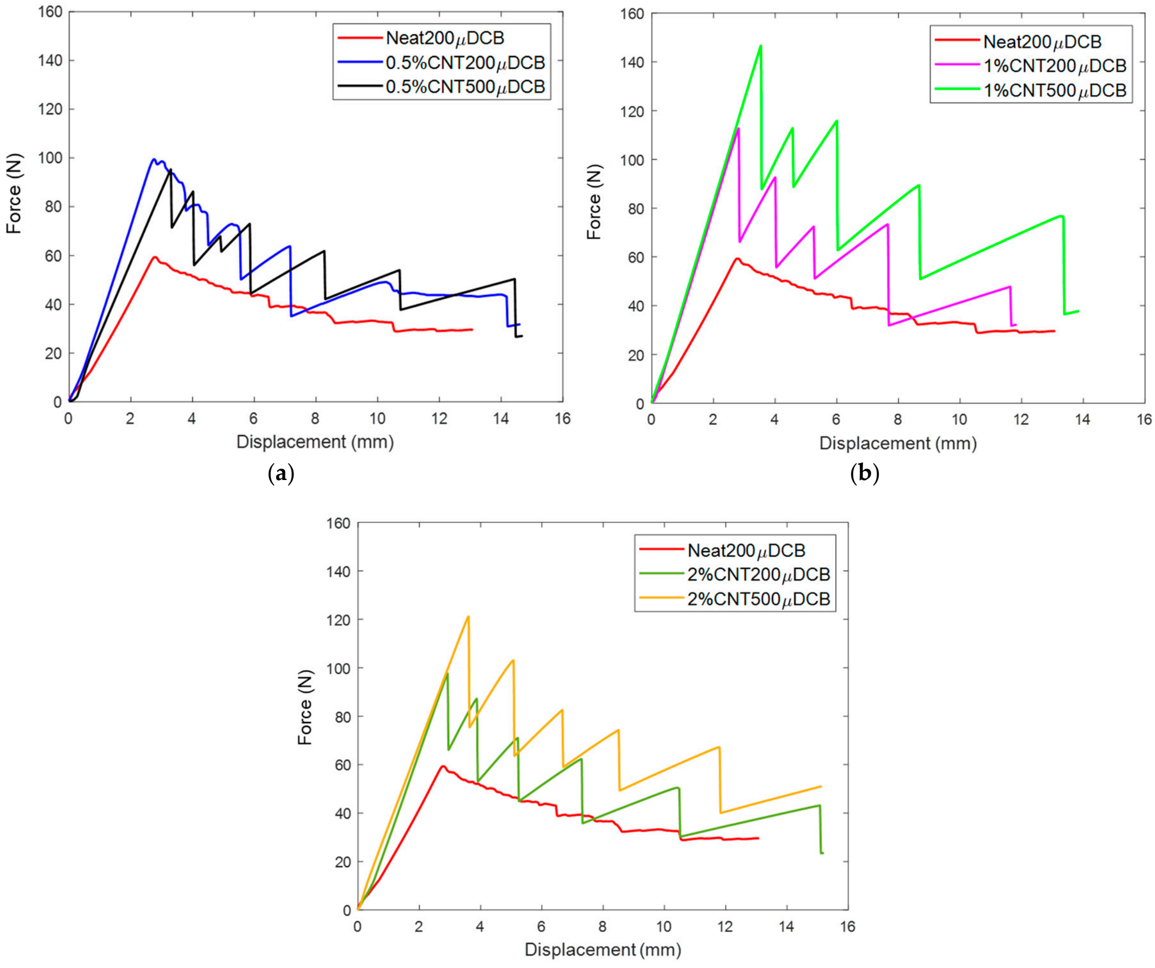

(**a**) (**b**)

(**c**)

Figure 4. Comparison of force-displacement curves from DCB tests with neat epoxy interleaves: (**a**) 0.5% wt. CNT interleaves; (**b**) 1% wt. CNT interleaves; and (**c**) 2% wt. CNT interleaves. Subfigures adapted from [19].

The slope of the first linear P-δ section remains fairly constant for a specific CNT wt. content but appears to become steeper with increasing CNT content, indicating higher flexural stiffness with nanoparticle concentration. The saw-tooth profiles of the curves in Figure 4 imply unstable crack growth followed by a strong arrest mechanism. The peak of each saw-tooth corresponds to the initiation load to propagate the crack at that specific crack length; however, the troughs of the saw-tooth indicate an arrest mechanism, subsequent to which the sample continues to behave 'elastically' with a reduced stiffness but with no change to the visible crack length until the next initiation load. The damage propagation in mode I for CNT interleaves can be described by a 'slip-stick' mechanism [22,23], where each sudden force drop in Figure 4 results in a crack slip/jump with a sudden increase in crack length. This slip is then arrested by a 'stick' phenomenon and held intact until the next slip event. The higher the force drops, the larger the crack slip tends to be.

Images from camera 1 were processed using MATLAB R2021b code (MathWorks, Boston, MA, USA) with the support of functions of the Image Processing toolbox. The acquired images were cropped, gray-scaled, binarized, and segmented to obtain the relevant sections and remove noise. The calibration index, which is a conversion measure of the number of pixels along a straight line to the actual distance in mm, was determined based on the two marked points, indicating a distance of exactly 40 mm, as described in Section 2.3. For each image, the code identified three points: one marked at the edge of the piano hinge, another marked at a 40 mm distance, and the final one marking the crack tip. The distance from the first point to the third point was calculated by counting the pixels along a straight and multiplying it by the calibration index. The known distance from the force application point to the end of the piano hinge of 2.3 mm was added to the calculated distance as a constant, yielding the instantaneous crack length. It is important to note that at large deformations, the curvature of the half-laminate would cause this measured crack length to be inaccurate. However, for the range of crack lengths considered in the tests, there were no significant discrepancies observed between the automatically determined crack length values and the visually measured crack lengths from camera 2. Owing to the stick–slip damage propagation, the evolution of crack length during the mode I test was discontinuous in nature. This is evidenced by the measured crack length remaining almost constant between force drop events. At every crack slip event corresponding to a force drop, a sudden discontinuous increase is observed in the measured crack length. However, despite the measured crack length remaining constant between consecutive force drops, a process zone evolves ahead of the crack tip, as described in Section 2.4.

3.1.2. Crack Arrest and Delay Mechanism

Although the mechanism of damage propagation is altered, the forces of crack arrest (troughs of the saw-tooth) are consistent with the forces in the baseline laminate containing the same interleaf thickness, i.e., each CNT-interleaved laminate containing a 200 μ interleaf possesses a P-δ profile that falls to the baseline 200 μ neat epoxy laminate P-δ profile at the end of a crack slip event. This is demonstrated by plotting an equivalent 'smooth crack propagation' curve based on the G_{Ic} computed from the crack initiation and the arrest loads, respectively, based on Equations (6) and (7). Essentially, the initiation G_{Ic}^{init} and arrest fracture toughness G_{Ic}^{arr} were computed from the initiation load P_{init} and arrest load P_{arr} for a stick–slip event from Equations (6) and (7). Subsequently, the equivalent smooth P-δ profiles were generated assuming linear elastic fracture mechanics for a stable crack. Figure 5 shows the actual force-displacement curve overlaid on the equivalent smooth propagation curves generated with the initiation and arrest toughness values, and the experimental data from the neat epoxy interleaf sample of the same thickness is overlaid on it. It is remarkable that the measured P-δ profile of crack growth in the neat epoxy interleaf overlaps almost identically with the crack arrest loads of a stick–slip damage propagation in a CNT interleaf of the same thickness. This implies that the arrest mechanisms are dictated by the presence and thickness of the interleaf, and the additional fracture toughness obtained is aided by CNT inclusion in the interleaf.

$$G_{Ic}^{init} = \frac{3P_{init}^{2}C_{init}^{2/3}}{2A_1bh} \tag{6}$$

$$G_{Ic}^{arr} = \frac{3P_{arr}^{2}C_{arr}^{2/3}}{2A_1bh} \tag{7}$$

The crack arrest forces are also predictable a priori if a neat epoxy interleaf can be tested first as this crack arrest seems to occur at a force nearly equal to that of a neat epoxy interleaved laminate of the same interleaf thickness. Therefore, a neat epoxy interleaf appears to set the lower bound for the force-displacement profile of a CNT-interleaved laminate.

In Figure 4, higher initiation loads as well as larger force drops (corresponding to larger crack jumps and higher kinetic energy release) can be observed at higher CNT wt. %, whereas increasing interleaf thickness shifts the force drop events (slips) to higher displacements. It is unsurprising that samples with a thicker interleaf exhibit higher peak initiation loads, arrest loads, as well as overall strain energy, but even after accounting for the larger thickness of the samples, higher fracture toughness is observed for the 500 μ interleaf samples. Comparing the laminates with the same CNT wt. content but different interleaf thicknesses in Figure 4a–c, it can be noted that the slip events are 'delayed' in the interfaces containing a thicker interleaf. This is evident from the fact that each force drop in the P-δ curve occurs at a higher displacement for the 500 μ interleaved samples when compared to their thinner interleaved equivalent. Thus, the damage propagation events appear to be delayed by the presence of a thicker interleaf.

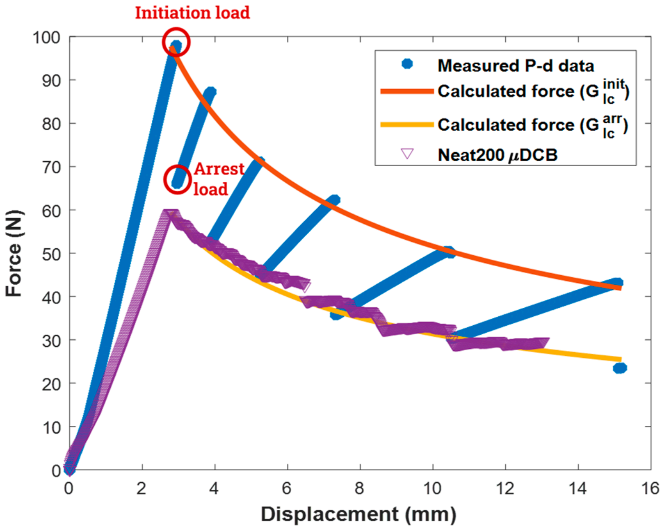

Figure 5. Equivalent smooth crack propagation curves of sample Neat200μDCB overlaid on the equivalent smooth crack propagation curves for sample 2%CNT200μDCB.

3.1.3. Fracture Toughness and R-Curve

Data in the literature place mode I fracture toughness for IM7/8552 composites in the range of 0.2–0.27 kJ/m^2 [24] when using different approaches to determine the critical load P_{crit} in Equation (1), such as visually observed deviations from linearity, or the 5% offset method described in ASTM D5528. Composite interfaces also exhibit a toughening effect on crack propagation owing to fiber bridging ahead of the crack front, generally represented by R-curves. As the crack length increases, more energy is required to further propagate the crack due to pinning and bridging effects between the fibers. The R-curves in Figure 6 represent the average fracture toughness values derived from multiple samples within a batch, along with the variations among them. It is important to note that the measured crack lengths after crack jumps are not consistent across all samples within a batch. Therefore, the available data of calculated G_{Ic} at measured crack lengths were interpolated at specific consistent values of crack lengths to yield the data in Figure 6.

In this study, the presence of an interleaf region does not allow for microscale fiber bridging across the fracture interface, thus resulting in no R-curve effect. This is a distinct difference from the approach of dispersing CNT into the entire matrix phase homogeneously, which could still allow for fiber bridging [25] and yet yield unstable crack propagation and reduction in the propagation fracture toughness.

A neat epoxy interleaf interacting with the crack front improves mode I initiation resistance to the range of 0.25–0.3 kJ/m^2 [4], according to a previous study by the authors. In this batch of Neat200μDCB samples, however, no statistical difference between the neat epoxy interleaf and a laminate with no interleaf is observed. A remarkable characteristic of interfaces containing an interleaf is the absence of any additional resistance as the crack length increases. The R-curves remain fairly flat in all cases, although significant gains in toughness are observed as a result of the addition of CNT to the interleaves. An increase in standard deviations in mode I critical interlaminar fracture toughness can be observed as the thickness of the interleaf is increased at every CNT concentration. This is potentially due to the formation of more three-dimensional process zones and the crack jumps not being along microscopically straight lines in the thicker interleaf laminates. However, a consistently larger standard deviation is observed in the 1%CNT500µDCB sample across all crack lengths. This is attributed to variability in manufacturing and one of the samples inherently possessing a lower fracture toughness compared to the other samples of the batch.

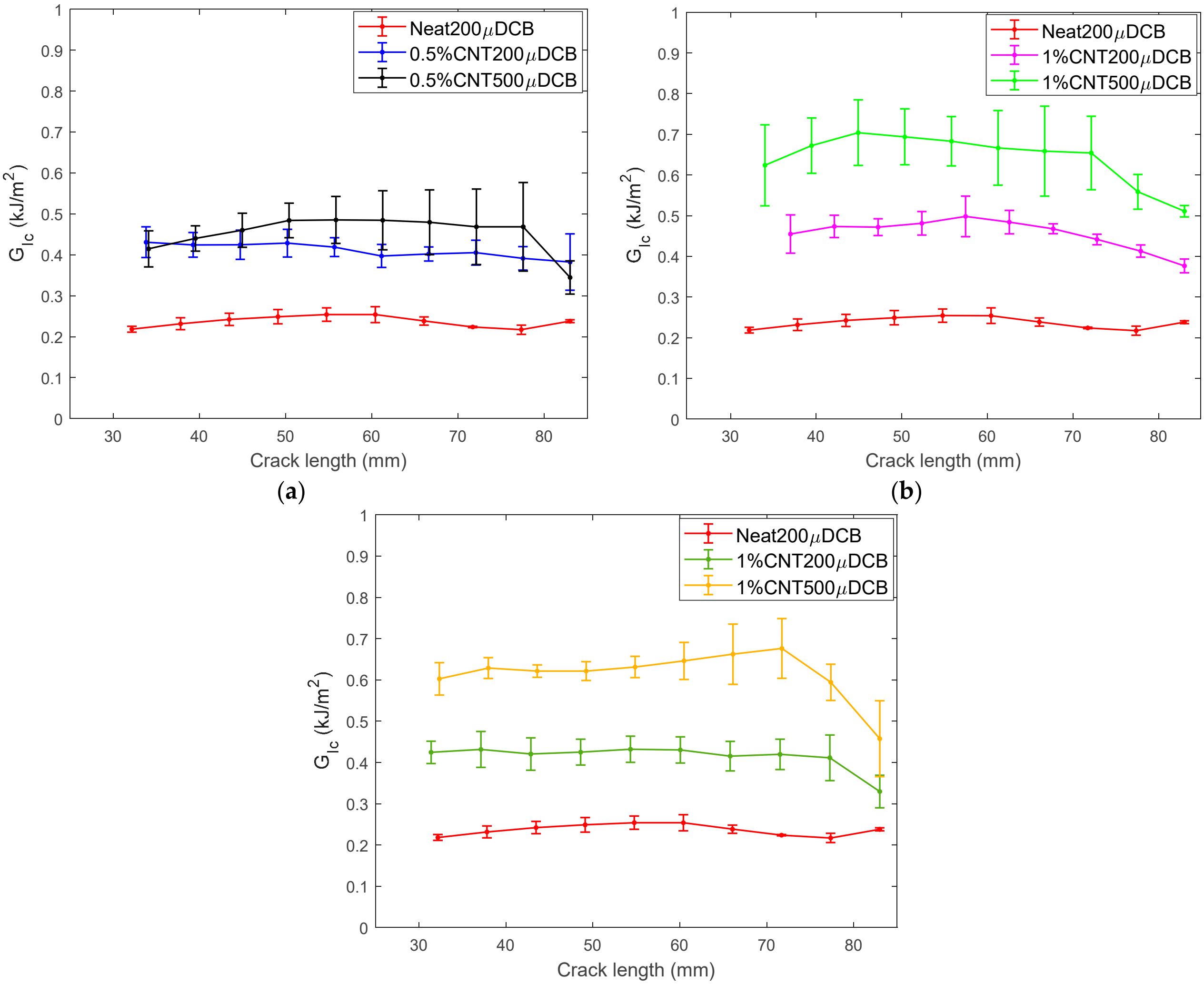

(**a**) (**b**)

(**c**)

Figure 6. R-curves from DCB tests compared to neat epoxy interleaves: (**a**) 0.5% CNT interleaves; (**b**) 1% CNT interleaves; and (**c**) 2% CNT interleaves.

No statistically significant difference can be observed in the fracture initiation and propagation resistance between laminates containing varying concentrations of CNT within a 200 µ interleaf across Figure 6a–c. This indicates that multiscale toughening mechanisms in mode I are triggered by the presence of CNT, but higher nanoparticle concentrations do not necessarily amplify these toughening mechanisms. The initiation toughness of the interleaved laminate improves nearly two times at even the lowest wt. concentration of CNT in Figure 6a and up to four times with CNT concentrations $\geq$ 1% wt. and an interleaf thickness of 500 µ in Figure 6b,c. This strengthens the evidence for interleaving nanoparticles as a superior approach to control interfacial toughness behavior compared to their homogenous dispersion in the entire matrix.

3.2. Mode II ENF Tests

The results of compliance calibration on non-pre-cracked specimens and the subsequent results from mode II fracture tests of pre-cracked specimens with an initial crack length of 30 mm are presented in the following section, further supported by insights from microscopy images.

Fracture Toughness and Crack Growth

The results from the initial compliance calibration for non-pre-cracked specimens and the corresponding coefficients are presented in Table 3. The results indicate a decrease in compliance C as crack length increases, aligning with expectations due to the applied force in the 3-point bending fixture affecting progressively damaged sections with increasing crack length. However, it is noteworthy that there is no statistically significant reduction in compliance between the neat epoxy interleaf samples and those with the inclusion of more CNT in the interleaf. This finding contrasts with the P-δ curves observed in mode I (Figure 4), which demonstrate an increase in slope/stiffness between neat and CNT-embedded interleaved samples.

Table 3. Compliance calibration coefficients from ENF tests.

Plate No.	**Sample Name**	**C (mm/N)**			**CC Coefficients**	
		a_0 = 20 mm	**a_0 = 30 mm**	**a_0 = 40 mm**	**M**	**A**
1	Neat200µENF	$0.0043 \pm 0.4 \times 10^{-3}$	$0.0031 \pm 0.2 \times 10^{-3}$	$0.0023 \pm 0.2 \times 10^{-3}$	3.54×10^{-8}	$0.0021 \pm 0.2 \times 10^{-3}$
2	0.5CNT200µENF	$0.0046 \pm 0.08 \times 10^{-3}$	$0.0033 \pm 0.07 \times 10^{-3}$	$0.0026 \pm 0.1 \times 10^{-3}$	3.66×10^{-8}	$0.0023 \pm 0.1 \times 10^{-3}$
3	0.5CNT500µENF	$0.0045 \pm 0.5 \times 10^{-3}$	$0.0030 \pm 0.18 \times 10^{-3}$	$0.0022 \pm 0.14 \times 10^{-3}$	4.05×10^{-8}	$0.0019 \pm 0.13 \times 10^{-3}$
4	1CNT200µENF	$0.0048 \pm 0.27 \times 10^{-3}$	$0.0035 \pm 0.16 \times 10^{-3}$	$0.0028 \pm 0.07 \times 10^{-3}$	3.54×10^{-8}	$0.0025 \pm 0.1 \times 10^{-3}$
5	1CNT500µENF	$0.0040 \pm 0.3 \times 10^{-3}$	$0.0027 \pm 0.17 \times 10^{-3}$	$0.0021 \pm 0.1 \times 10^{-3}$	3.49×10^{-8}	$0.0018 \pm 0.1 \times 10^{-3}$
6	2CNT200µENF	$0.0042 \pm 0.2 \times 10^{-3}$	$0.0030 \pm 0.15 \times 10^{-3}$	$0.0024 \pm 0.08 \times 10^{-3}$	3.24×10^{-8}	$0.0021 \pm 0.08 \times 10^{-3}$
7	2CNT500µENF	$0.0039 \pm 0.2 \times 10^{-3}$	$0.0026 \pm 0.11 \times 10^{-3}$	$0.0020 \pm 0.09 \times 10^{-3}$	3.40×10^{-8}	$0.0017 \pm 0.08 \times 10^{-3}$

Figure 7 illustrates the P-δ curves derived from fracture tests on pre-cracked samples. Note that the forces and displacements in the ENF tests are compressive, but here, they are indicated by a positive sign. The P-δ curve of the neat epoxy interleaf is smooth and the trend is consistent with steady crack front advancement, as explained in the ASTM D7905. This confirms that the propagation of the crack through the neat epoxy interleaf is steady in both modes I and II. In contrast, the CNT interleaf samples once again exhibit unsteady crack growth, with the exception of the 500 µ interleaves. Notably, in the 200 µ interleaves, there is little non-linearity in the curve leading up to the maximum force P_{max} and a large force drop right after, indicative of a sudden crack jump. The 500 µ interleaf samples, however, display some non-linearity leading up to P_{max}, suggesting the formation of a large damage process zone and crack growth in the interior front. At higher CNT loading (1% wt. and 2% wt.), a smooth crack growth region is also inferred from the lack of a force drop event. However, at the end of these crack jumps/force drop events, the crack length often exceeds 50 mm, extending beyond the point of force application, making the continuation of the test infeasible. As a result, generating an R-curve for this test is impractical due to insufficient data points at various crack lengths to measure the toughness.

Consequently, attention is solely directed towards the determination of mode II critical initiation toughness, calculated using Equation (5), and the values are plotted in Figure 8. The findings reveal an interesting interplay between interleaf thickness and CNT concentration concerning mode II critical initiation toughness. Notably, in the 200 µ case, the impact of CNT inclusion is immediately apparent from a large increase in mode II toughness. However, adding low CNT wt.% to a thick interleaf appears to have a detrimental effect on toughness. At low CNT loading levels, a thinner interleaf seems to offer more resistance to crack progression. In contrast, at CNT concentrations above 1%, consistent improvements are observed for both thicknesses compared to the neat epoxy interleaf. Remarkably, there is an optimum CNT concentration observed for the 200 μ interleaf at 1%, offering the highest critical initiation toughness, but the thicker 500 μ interleaf allows for higher CNT loading levels with continued improvement of damage resistance. This is logical as the thicker interleaf allows for a three-dimensional network of dispersed CNT, whereas the thin interleaf may be more spatially limited, and overloading CNT concentrations could lead to poor dispersion (agglomeration) and interphase adhesion. This underscores the intricate relationship between CNT concentration and interleaf thickness in influencing the mode II critical initiation toughness of the material.

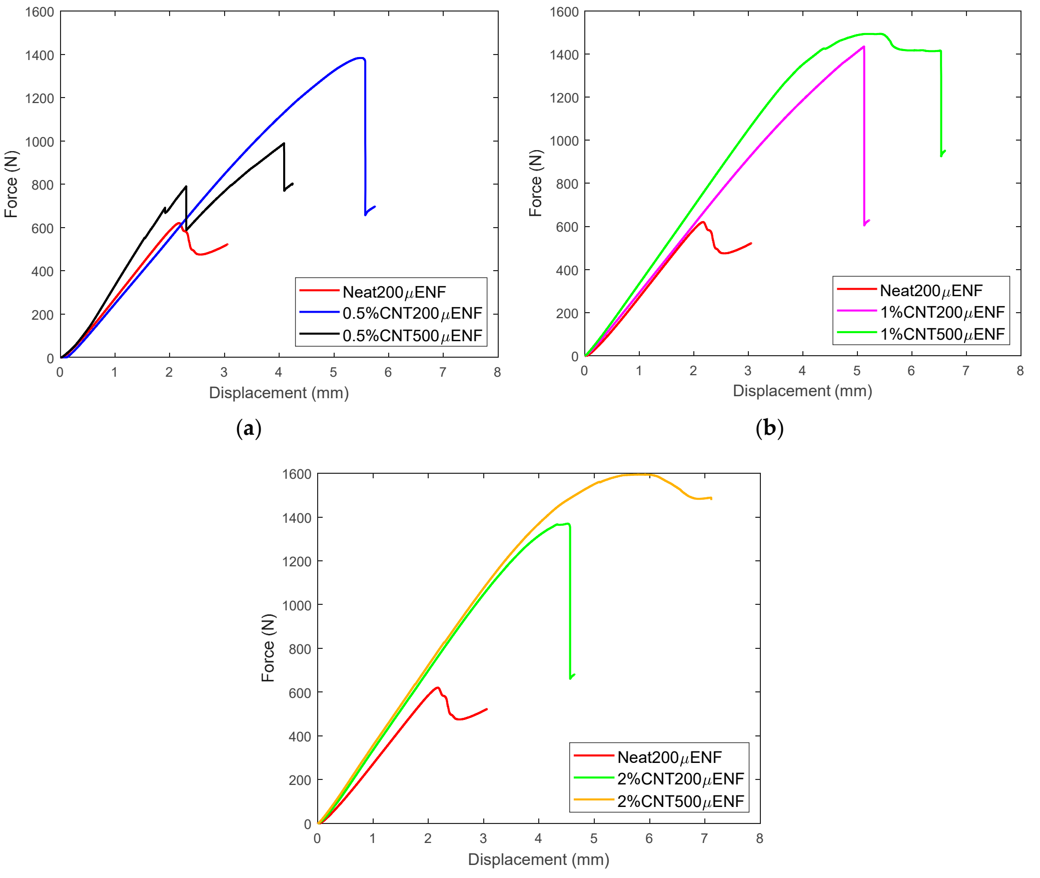

(**a**) (**b**)

(**c**)

Figure 7. Force-displacement curves from ENF tests: (**a**) 0.5% CNT interleaves; (**b**) 1% CNT interleaves; and (**c**) 2% CNT interleaves.

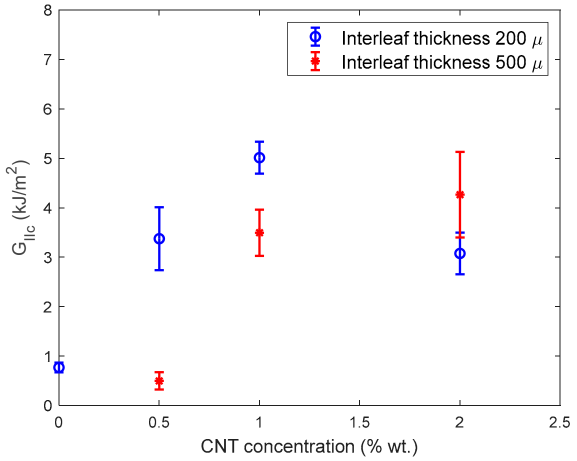

Figure 8. Critical shear mode II strain energy release rate from ENF tests of various CNT concentrations and interleaf thicknesses.

3.3. Fractography

Microstructural characterization with a Keyence Laser Scanning Confocal microscope showed that upon compaction in the autoclave, the 200 μ interleaves resulted in an actual uniform thickness of around 150 μ, whereas the 500 μ interleaves compacted to around 370–400 μ thickness. Micrographs obtained via a Keyence VR-5000 wide-area 3D measurement microscope (Keyence Corporation, Osaka, Japan), as shown in Figure 9, also display higher tortuosity to the crack path and undulations in the interface for thicker interleaves. The mean striation height along the crack path in the 200 μ interleaf samples is 60 μ. The undulations in the micrographs confirm cohesive-dominated failure in the thicker interleaf while suggesting a mix of adhesive and cohesive failure regions in Figure 9a, as illustrated by small regions of adhesive peeling. Furthermore, Figure 9b reveals that the waviness of the undulations is clustered close to the mid-line (shorter wavelengths with a mean amplitude of 110 μ), and they become sparser (longer wavelengths with a mean amplitude of 170 μ) towards the edge of the specimen. This indicates that the delamination front is not a straight line but curved and quasi-parabolic. The striations, as well as the post-processed images from both cameras, confirm that the crack length is nearly equal on both edges during the test, thus implying that the quasi-parabolic crack front is symmetrical.

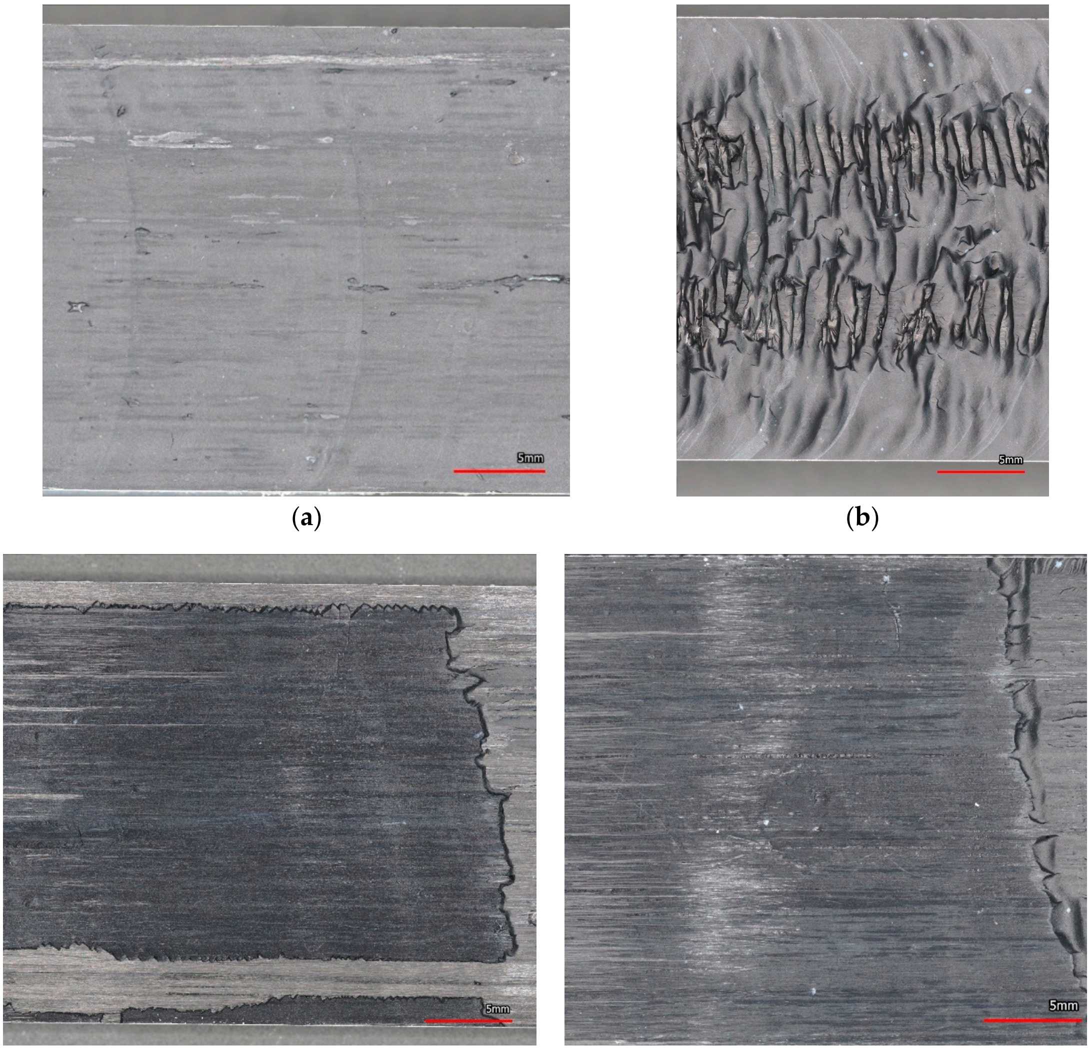

(**a**) (**b**)

(**c**) (**d**)

Figure 9. Fracture striations and undulations on failed surfaces: (**a**) 2%CNT200μDCB; (**b**) 2%CNT500μDCB; (**c**) 2%CNT200μENF; and (**d**) 2%CNT500μENF. Scale markers depict a distance of 5 mm.

Scanning electron microscopy (SEM) was performed with the JEOL JSM-7500F Field Emission microscope on 5 mm by 5 mm samples carefully cut out of the fracture surfaces with a diamond saw. Although CNT are conductive, the samples were coated with a thin layer (8 nm) of gold nanoparticles via sputtering under vacuum. The micrographs reveal integral details about the nature of microscale and nanoscale damage mechanisms upon crack propagation. Figure 10a is at the micro scale, displaying fiber matrix debonding at a small region of adhesive peeling that exposed the fiber underneath, and Figure 10b shows a higher magnification view of the undulations observed in Figure 10b. These undulations, viewed through SEM, show even smaller and clustered crimps existing within the overall wavy ridges seen via the 3D surface profiler, signaling the role of multiscale crack path tortuosity in the toughening behavior. The presence of exposed CNT on fracture flake edges confirms that they are debonded from the interleaf matrix they were originally embedded within, as can be seen in Figure 10c,d. The frayed CNT on the broken flakes indicate that there was considerable load transfer between the matrix and nanoparticles that resulted in CNT pullout from the host polymer. This nanoscale mechanism adds to the total energy required to propagate a crack, thus improving the overall toughness of the interface. In Figure 10e,f, a CNT network that dissociated upon direct interaction with the crack front during damage propagation is depicted. The dissociated network exposes the nanotubes that have been stretched along the longitudinal direction, suggesting that the mechanical capabilities of the CNT have been maximally leveraged at the interface.

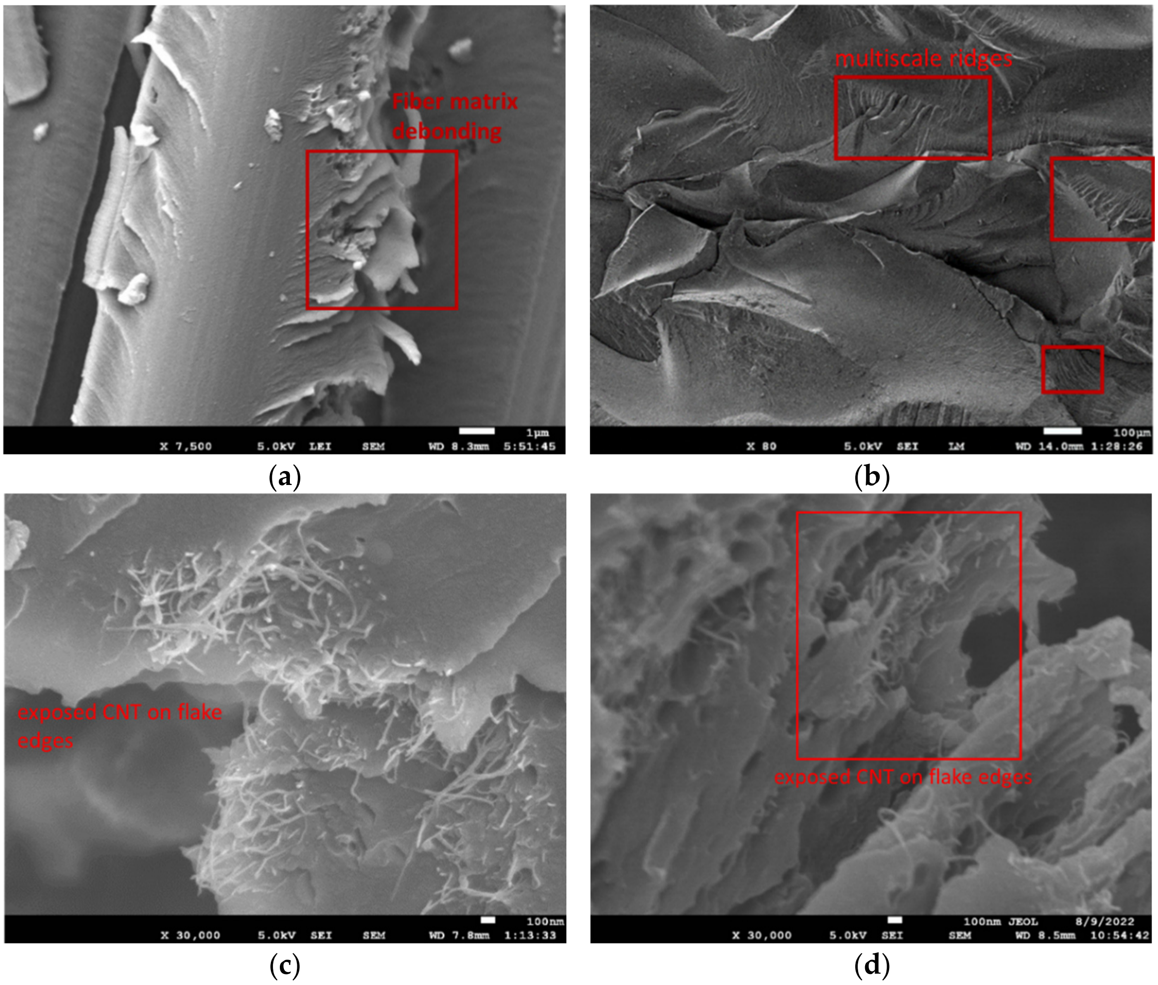

Figure 10. *Cont.*

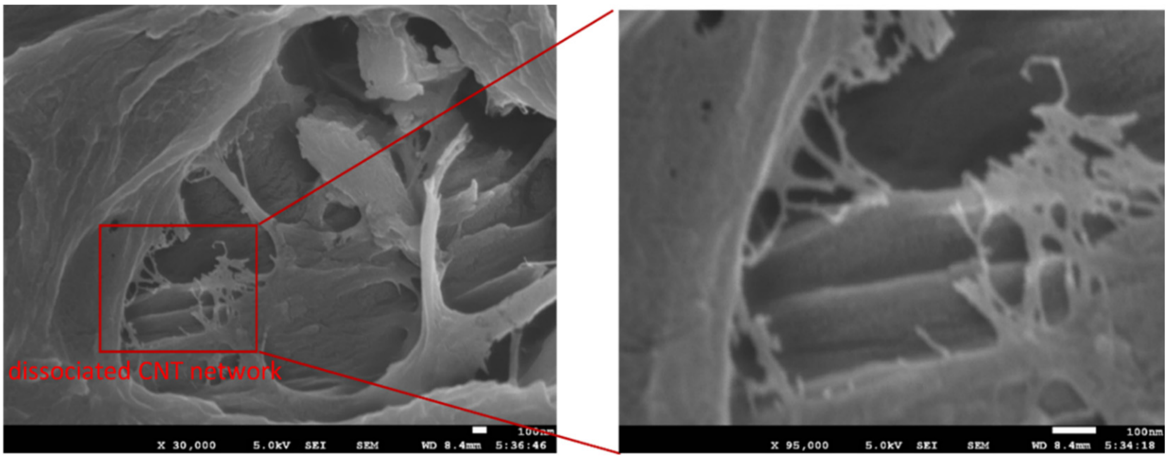

(**e**) (**f**)

Figure 10. SEM images of fracture surfaces: (**a**) debonding of carbon fiber from interleaf polymer (scale marker: 1 µm, 7500× zoom); (**b**) undulations/ridges at the micro scale (scale marker: 100 µm, 80× zoom); (**c**) CNT debonding at a fracture flake edge (scale marker: 1 nm, 30,000× zoom); (**d**) micrograph showing the participation of the CNT at fracture striations (scale marker: 1 nm, 30,000× zoom); (**e**) CNT network dissociation upon crack propagation (scale marker: 1 nm, 30,000× zoom); and (**f**) zoomed-in image of the dissociated CNT network (scale marker: 1 nm, 95,000× zoom).

Based on the observations from the DCB and ENF specimens, the fracture mechanisms differ significantly between the two. In DCB specimens, the primary mechanisms included microscale crack path tortuosity, macroscale striations, and the dissociation of CNT networks, all of which contribute to enhanced toughness by absorbing energy and resisting crack propagation. In contrast, ENF specimens predominantly exhibit CNT pullout and debonding, which adds the most resistance to crack growth through high-energy processes, thus also explaining why mode II critical initiation toughness improved up to six times in CNT-interleaved samples.

4. Conclusions

This study focused on the targeted incorporation of partially cured interleaves containing nanoparticles in the composite consolidation process and its effectiveness on fracture resistance at co-cured interfaces. The addition of nanoparticles to the interleaf resulted in a higher stiffness of the samples, as expected. The highest values of mode I interlaminar fracture toughness and mode II shear fracture toughness were about 0.7 $\mathrm{kJ/m^2}$ and 5 $\mathrm{kJ/m^2}$, respectively, for a CNT concentration of 1% wt. Additionally, the force-displacement data as well as micrographs of failed surfaces revealed a notable change in the underlying damage mechanisms governing crack propagation in modes I and II due to CNT interleaves.

Two remarkable aspects stood out from the mode I test results. First, a slip–stick damage progression phenomenon was observed with a predictable crack arrest load for a CNT interleaf based on the force-displacement profile of a neat epoxy interleaf of the same thickness. This confirmed that the initiation interlaminar toughness is improved by controlling CNT concentration to induce nanoscale debonding, and arrest toughness can be controlled via the interleaf thickness to induce microscale crack path tortuosity and larger process zones. Second, a damage delay phenomenon of each slip event occurred as a function of interleaf thickness. The overall results confirm that crack growth processes are altered and toughened in mode I at three scales due to nanoparticle interleaving: at the macro scale via slip–stick-based jump, at the micro scale through crack path tortuosity behind the quasi-parabolic crack front, and at the nano scale through CNT networks interacting directly with the crack front.

The mode II results highlight the interplay between CNT inclusion and interleaf thickness with the existence of optimum CNT concentration to enable three-dimensional nanoscale networks. Significant damage resistance in mode II is added via CNT debonding and pullout events, which require high amounts of energy.

The coalition of these multiscale toughening mechanisms within the interleaved interface enables the design of co-cured composite joints with superior toughness for aeronautics applications.

Author Contributions: N.S.: Conceptualization, Methodology, Data collection, Writing—original draft preparation, Writing—review and editing, Funding acquisition, and Project administration. C.B.: Conceptualization, Writing—review and editing, Supervision, Project administration, and Funding acquisition. All authors have read and agreed to the published version of the manuscript.

Funding: This project has received funding from the European Union's Horizon 2020 research and innovation program under the Marie Skłodowska-Curie grant agreement No. 835672, MACADAMIA.

Data Availability Statement: The authors state that the data supporting the findings of this study are available within the article. Raw data will be made available upon request.

Acknowledgments: The authors acknowledge the support from the Delft Aerospace Materials and Structures Lab (DASML), particularly Alexander Uithol, to conduct experiments and post-process image data. This article is a revised and expanded version of a paper titled "Damage Arrest Mechanisms in Nanoparticle Interleaved Composite Interfaces", which was presented at ECCM20, Lausanne, June 2022.

Conflicts of Interest: The authors declare that they have no known competing financial interests or personal relationships that could have appeared to influence the work reported in this paper.

References

1. Fernandes, R.L.; Budzik, M.K.; Benedictus, R.; de Freitas, S.T. Multi-material adhesive joints with thick bond-lines: Crack onset and crack deflection. *Compos. Struct.* **2021**, *266*, 113687. [CrossRef]
2. Mohan, J.; Ivanković, A.; Murphy, N. Mode I fracture toughness of co-cured and secondary bonded composite joints. *Int. J. Adhes. Adhes.* **2014**, *51*, 13–22. [CrossRef]
3. Dhilipkumar, T.; Rajesh, M. Enhancing strength and stiffness of composite joint through co-cure technique. *Compos. Commun.* **2021**, *27*, 100878. [CrossRef]
4. Subramanian, N.; Bisagni, C. Multiscale Damage in Co-Cured Composites—Perspectives from Experiments and Modelling. In Proceedings of the 36th Technical Conference of the American Society for Composites 2021, College Station, TX, USA, 20–22 September 2021.
5. Marino, S.G.; Czél, G. Improving the performance of pseudo-ductile hybrid composites by film-interleaving. *Compos. Part A Appl. Sci. Manuf.* **2021**, *142*, 106233. [CrossRef]
6. Quan, D.; Farooq, U.; Zhao, G.; Dransfeld, C.; Alderliesten, R. Co-cured carbon fibre/epoxy composite joints by advanced thermoplastic films with excellent structural integrity and thermal resistance. *Int. J. Adhes. Adhes.* **2022**, *118*, 103247. [CrossRef]
7. Subramanian, N.; Rai, A.; Chattopadhyay, A. Atomistically informed stochastic multiscale model to predict the behavior of carbon nanotube-enhanced nanocomposites. *Carbon* **2015**, *94*, 661–672. [CrossRef]
8. Latif, Z.; Ali, M.; Lee, E.-J.; Zubair, Z.; Lee, K.H. Thermal and Mechanical Properties of Nano-Carbon-Reinforced Polymeric Nanocomposites: A Review. *J. Compos. Sci.* **2023**, *7*, 441. [CrossRef]
9. Fard, M.Y. Carbon nanotube network and interphase in buckypaper nanocomposites using atomic force microscopy. *Int. J. Mech. Sci.* **2021**, *212*, 106811. [CrossRef]
10. Palmieri, B.; Siviello, C.; Petriccione, A.; Espresso, M.; Giordano, M.; Martone, A.; Cilento, F. Mechanical and Viscoelastic Properties of Carbon Fibre Epoxy Composites with Interleaved Graphite Nanoplatelet Layer. *J. Compos. Sci.* **2023**, *7*, 235. [CrossRef]
11. Abidin, M.S.Z.; Herceg, T.; Greenhalgh, E.S.; Shaffer, M.; Bismarck, A. Enhanced fracture toughness of hierarchical carbon nanotube reinforced carbon fibre epoxy composites with engineered matrix microstructure. *Compos. Sci. Technol.* **2018**, *170*, 85–92. [CrossRef]

12. Mousavi, S.R.; Estaji, S.; Paydayesh, A.; Arjmand, M.; Jafari, S.H.; Nouranian, S.; Khonakdar, H.A. A review of recent progress in improving the fracture toughness of epoxy-based composites using carbonaceous nanofillers. *Polym. Compos.* **2022**, *43*, 1871–1886. [CrossRef]
13. Liu, Q.; Lomov, S.V.; Gorbatikh, L. The interplay between multiple toughening mechanisms in nanocomposites with spatially distributed and oriented carbon nanotubes as revealed by dual-scale simulations. *Carbon* **2018**, *142*, 141–149. [CrossRef]
14. Khalid, M.Y.; Kamal, A.; Otabil, A.; Mamoun, O.; Liao, K. Graphene/epoxy nanocomposites for improved fracture toughness: A focused review on toughening mechanism. *Chem. Eng. J. Adv.* **2023**, *16*, 100537. [CrossRef]
15. Subramanian, N.; Koo, B.; Venkatesan, K.R.; Chattopadhyay, A. Interface mechanics of carbon fibers with radially-grown carbon nanotubes. *Carbon* **2018**, *134*, 123–133. [CrossRef]
16. Liu, Q.; Lomov, S.V.; Gorbatikh, L. Enhancing Strength and Toughness of Hierarchical Composites through Optimization of Position and Orientation of Nanotubes: A Computational Study. *J. Compos. Sci.* **2020**, *4*, 34. [CrossRef]
17. Shin, Y.C.; Lee, W.I.; Kim, H.S. Mode II interlaminar fracture toughness of carbon nanotubes/epoxy film-interleaved carbon fiber composites. *Compos. Struct.* **2020**, *236*, 111808. [CrossRef]
18. Ni, X.; Acauan, L.H.; Wardle, B.L. Coherent nanofiber array buckling-enabled synthesis of hierarchical layered composites with enhanced strength. *Extreme Mech. Lett.* **2020**, *39*, 100773. [CrossRef]
19. Subramanian, N.; Bisagni, C. Damage Arrest Mechanisms in Nanoparticle Interleaved Composite Interfaces. In *20th European Conference on Composite Materials, Volume 3—Characterization*; EPFL Lausanne, Composite Construction Laboratory: Lausanne, Switzerland, 2022; pp. 255–264.
20. *ASTM D5528-13*; Test Method for Mode I Interlaminar Fracture Toughness of Unidirectional Fiber-Reinforced Polymer Matrix Composites. D30 Committee, ASTM International: West Conshohocken, PA, USA, 2022. [CrossRef]
21. *ASTM D7905/D7905M-14*; Test Method for Determination of the Mode II Interlaminar Fracture Toughness of Unidirectional Fiber-Reinforced Polymer Matrix Composites. D30 Committee, ASTM International: West Conshohocken, PA, USA, 2019. [CrossRef]
22. Zhou, Y.; Xiao, Y.; Wu, Q.; Xue, Y. A multi-state progressive cohesive law for the prediction of unstable propagation and arrest of Mode-I delamination cracks in composite laminates. *Eng. Fract. Mech.* **2021**, *248*, 107684. [CrossRef]
23. Guo, S.; Xia, Y.; Wei, X.; Zhou, Q. Investigation on the stable and stick-slip crack propagation behaviors in double cantilever beam test. *J. Adhes.* **2019**, *96*, 1198–1218. [CrossRef]
24. Raimondo, A.; Oca, I.U.; Bisagni, C. Influence of interface ply orientation on delamination growth in composite laminates. *J. Compos. Mater.* **2021**, *55*, 3955–3972. [CrossRef]
25. Chaudhry, M.; Czekanski, A.; Zhu, Z. Characterization of carbon nanotube enhanced interlaminar fracture toughness of woven carbon fiber reinforced polymer composites. *Int. J. Mech. Sci.* **2017**, *131–132*, 480–489. [CrossRef]